


Intrinsic and extrinsic spin-orbit coupling and spin relaxation in monolayer PtSe₂Marcin Kurpas ^{*}*Institute of Physics, University of Silesia in Katowice, 41-500 Chorzów, Poland*Jaroslav Fabian *Institute for Theoretical Physics, University of Regensburg, Regensburg 93040, Germany* (Received 8 June 2020; revised 5 February 2021; accepted 22 February 2021; published 5 March 2021)

Monolayer PtSe₂ is a semiconducting transition-metal dichalcogenide characterized by an indirect band gap, space inversion symmetry, and high carrier mobility. Strong intrinsic spin-orbit coupling and the possibility to induce extrinsic spin-orbit fields by gating make PtSe₂ attractive for fundamental spin transport studies as well as for potential spintronics applications. We perform a systematic theoretical study of the spin-orbit coupling and spin relaxation in this material. Specifically, we employ first-principles methods to obtain the basic orbital and spin-orbital properties of PtSe₂, also in the presence of an external transverse electric field. We calculate the spin mixing parameters b^2 and the spin-orbit fields Ω for the Bloch states of electrons and holes. This information allows us to predict the spin lifetimes due to the Elliott-Yafet and D'yakonov-Perel mechanisms. We find that b^2 is rather large, on the order of 10^{-2} and 10^{-1} , while Ω varies strongly with doping, being about 10^3 – 10^4 ns⁻¹ for carrier density in the interval 10^{13} – 10^{14} cm⁻² at the electric field of 1 V/nm. We estimate the spin lifetimes to be on the picosecond level.

DOI: [10.1103/PhysRevB.103.125409](https://doi.org/10.1103/PhysRevB.103.125409)**I. INTRODUCTION**

Transition-metal dichalcogenides (TMDs) have been investigated—mainly in the bulk form but also as layered slabs—for many decades [1–5]. The recent revival of interest in TMDs has been fueled by a broad range of fascinating electronic, optical, and spin properties of two-dimensional (2D) samples of TMDs, which are stable in air. The possibility of controlling physical properties of TMDs by, e.g., stacking [6–11], doping [12], straining [13,14], or gating [15], demonstrates their potential for electronic [16], optoelectronic [17], and valleytronics [18] applications. Moreover, due to strong spin-orbit coupling and the presence of a semiconducting gap, TMDs are also well suited for applications in spintronics [19,20], as they can induce spin-orbit coupling (SOC) into graphene via a strong proximity effect [21,22].

Recently demonstrated atomically thin PtSe₂ [23,24] is a distinct member of the 2D TMD family. What sharply distinguishes this material from other TMDs is its high room-temperature carrier mobility [25], which is close to that of phosphorene [26]. But in contrast to phosphorene, PtSe₂ exhibits good stability when exposed to air [25]. Like other TMDs, a monolayer of PtSe₂ consists of an atomically thin layer of transition-metal (Pt) within two layers of chalcogen (Se) atoms [Figs. 1(a) and 1(b)]. It crystallizes in the centrosymmetric structure of the $P3\bar{m}1$ space group being isomorphic with the D_{3d} point group. While bulk PtSe₂ is metallic, in the monolayer limit it is a semiconductor with a

sizeable indirect gap reported to be in the range of 1.2–2 eV [10,25,27–29].

Monolayer PtSe₂ also holds promise to exhibit rich spin phenomena. One of the most exciting is the hidden spin polarization [30] of degenerate bands near the Fermi level, recently observed in angle-resolved photoemission spectroscopy (ARPES) experiments [31]. Its origin is attributed to the local site dipole fields (local Rashba effect) generating opposite helical spin textures for spin degenerate states, spatially resolved with respect to different Se layers. The opposite dipole fields compensate each other, leaving the total crystal potential inversion symmetric and thus preserving the spin degeneracy of bands [30]. Another interesting phenomenon is the defect-induced magnetism, which is reported for mono- [32,33] and multilayer [11] PtSe₂ slabs. In the latter case, a magnetic phase can be switched between ferro- to antiferromagnetic by changing the parity of the number of layers [11]. The interplay of such magnetic effects with spin-orbit coupling could lead to interesting magnetotransport phenomena.

Strong spin-orbit coupling, intrinsic band gap, and high carrier mobility make PtSe₂ a good candidate for building spintronic devices, such as a spin valve or spin transistor [34]. Essential for these devices is a coherent (ensemble) dynamics of the electron spin. Such a dynamics is disrupted by spin dephasing and spin relaxation processes. Thus the question concerning the electron spin lifetime in monolayer PtSe₂ is of great importance for potential applications of this material in spintronics. This question has not yet been systematically addressed theoretically or experimentally.

Here we investigate the problem of the spin relaxation in monolayer PtSe₂ by employing first-principles calculations and extracting useful information about the spin-orbit

^{*}marcin.kurpas@us.edu.pl

coupling and spin relaxation. Two mechanisms dominating spin relaxation in nonmagnetic materials, such as PtSe₂, are considered. Namely, the Elliott-Yafet [35,36] and D'yakonov-Perel [37,38]. In the Elliott-Yafet mechanism, the intrinsic SOC mixes opposite spin components of degenerate Bloch states. In effect, an electron can flip its spin upon momentum scattering, with the probability given by the so-called *spin mixing* parameter $b_{\mathbf{k}}^2$. It is related to spin relaxation time $\tau_{s,EY}$ via the formula [35,39,40]

$$\tau_{s,EY}^{-1} \approx 4b^2\tau_p^{-1}, \quad (1)$$

where τ_p^{-1} is the momentum relaxation rate, and b^2 is the Fermi surface average of $b_{\mathbf{k}}^2$.

Another contribution to the Elliott-Yafet mechanism could come from heavy impurities, which could easily dominate spin-flip scattering if they provide strong-enough local SOC [19]. We do not study such impurities in this paper, as this would require the knowledge of the specific scatterer. Rather, we establish what the minimum spin relaxation would be if scattering is dominated by phonons and/or light impurities.

In the D'yakonov-Perel mechanism spins randomize their phase via the interaction with the fluctuating Rashba fields Ω_k . These fields appear due to broken space inversion symmetry of the structure, e.g., due to a substrate or an external electric field. The initial phase of spins is completely randomized after the time $\tau_{s,DP}$,

$$\tau_{s,DP}^{-1} = \Omega_{\perp}^2 \tau_p, \quad (2)$$

where Ω_{\perp}^2 denotes the Fermi surface average of the squared spin-orbit field component $\Omega_{\mathbf{k}\perp}^2$ being perpendicular to the spin orientation. In realistic systems these two mechanisms usually coexist and compete with each other. Here we show that for both mechanisms the spin relaxation in PtSe₂ is very fast, up to a few picoseconds for experimentally accessible momentum scattering time. Thus PtSe₂ does not appear to be the best material for building spintronic devices requiring long spin lifetimes. However, it should be useful for investigating spin-orbit-induced transport phenomena.

The paper is organized as follows. In Sec. II we briefly describe methods and details of calculations. Section III contains results of our first-principles calculations with a discussion, including effects of the intrinsic and extrinsic SOC on the band structure, spin mixing parameter, and spin-orbit fields. Estimations of spin lifetime due to Elliott-Yafet and D'yakonov-Perel relaxation mechanisms and comparison are also included here. Section IV contains final conclusions.

II. METHODS

First-principles calculations were performed using the QUANTUM ESPRESSO package [41,42]. The norm-conserving pseudopotential with the Perdew-Burke-Ernzerhof (PBE) [43] version of the generalized gradient approximation (GGA) exchange-correlation functional was used. Calculations with a hybrid functional were done with the Heyd-Scuseria-Ernzerhof (HSE) [44] functional, with the admixture parameters chosen to fit the recently predicted values of the band gap [10,45].

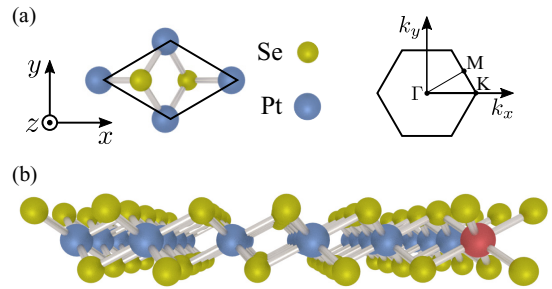


FIG. 1. Sketch of the crystalline structure of monolayer PtSe₂. (a) Top view on the unit cell and the corresponding first Brillouin zone with indicated high-symmetry points. (b) Side view of the atomic structure of monolayer PtSe₂. The center of inversion is at the Pt atom, marked red.

The kinetic energy cutoff of the plane-wave basis sets was 50 Ry for the wave function and 200 Ry for charge density. These values were found to give converged results also for spin-related quantities. To avoid spurious interactions between the copies of PtSe₂ monolayer, a vacuum of 20 Å was introduced and was increased to 21.5 Å when the electric field was turned on. Calculations with electric field were done with the dipole correction [46]. Self-consistency was achieved with $21 \times 21 \times 1$ Monkhorst-Pack grid, while for structure optimization a smaller grid $10 \times 10 \times 1$ was chosen. The initial lattice constant of PtSe₂ was taken from experiment [23] and was later optimized for the chosen pseudopotential using the variable cell and quasi-Newton schemes as implemented in the QUANTUM ESPRESSO package. During optimization process all atoms were free to move in all directions to minimize the internal forces below the threshold 10^{-4} Ry/bohr. The calculated lattice constant is $a = 3.748$ Å, very close to the experimental value in bulk 3.73 Å [23], and is in good agreement with other calculations [29,32].

The Fermi contour averages of spin mixing parameter b^2 and spin-orbit field Ω^2 entering the formulas (1) and (2) were calculated using the formula

$$A = \frac{1}{\rho(E_F)S_{BZ}} \int_{FC} \frac{A_{\mathbf{k}}}{\hbar|\mathbf{v}_F(\mathbf{k})|} dk, \quad (3)$$

where $A_{\mathbf{k}}$ stands for $b_{\mathbf{k}}^2$ or $\Omega_{\mathbf{k}\perp}^2$, S_{BZ} is the area of the Fermi surface, $\rho(E_F)$ is the density of states per spin at the Fermi level, $\mathbf{v}_F(\mathbf{k})$ is the Fermi velocity, and the integration takes over an isoenergy contour.

III. RESULTS AND DISCUSSION

We first examine the orbital effects. The calculated nonrelativistic and relativistic band structures are shown in Fig. 2(a). Monolayer PtSe₂ is an indirect-gap semiconductor with a sizable band gap. Without SOC the calculated band gap is 1.38 eV. The valence-band (VB) maximum is located slightly away (0.15 Å⁻¹) from the Brillouin-zone (BZ) center, while the conduction-band (CB) minimum lies in the middle of the ΓM path. The band edge at the Γ point is a saddle point lying 38 meV below the global VB maximum [see the inset in Fig. 2(a)]. The valence and conduction bands close to the band gap are formed mainly by *d* electrons of platinum and

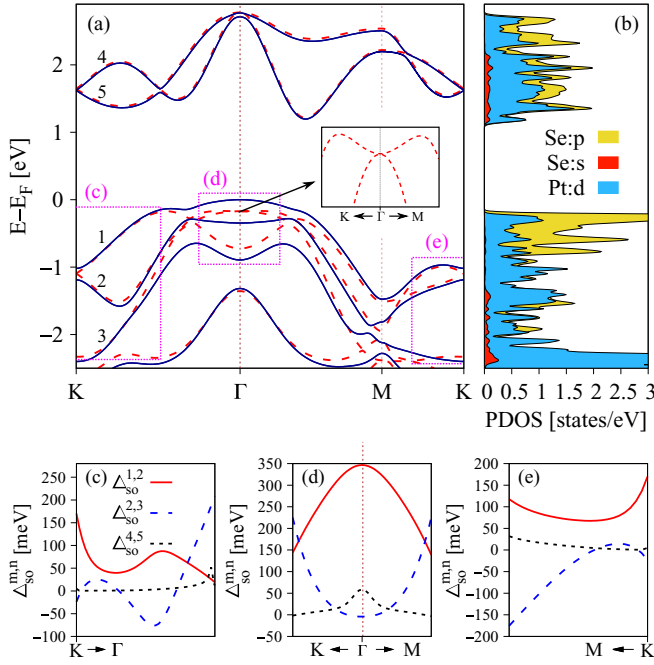


FIG. 2. (a) Calculated non-relativistic (dashed line) and relativistic (solid line) band structures along high symmetry lines in the FBZ. The nonrelativistic band structure is misaligned with the Fermi energy for better transparency. The inset shows a zoom of bands close to the Γ point. Purple rectangles depict the range of k points in (c)–(e). (b) Density of states projected onto atomic orbitals. (c)–(e) Extracted spin-orbital splittings $\Delta_{so}^{n,m}$ between the valence bands m and n , labeled 1,2,3, and 4,5 in (a), calculated as a difference between interband energy distances with SOC and without SOC.

p electrons of selenium [Fig. 2(b)]. In the valence band up to 1 eV below the Fermi level the dominant contribution comes from Se p electrons, with significant admixture of d electrons from Pt. In the conduction band the contributions from Pt and Se atoms are almost equal.

A. Intrinsic spin-orbit coupling

Spin-orbit splitting. Relativistic effects in PtSe₂ are significant. Spin-orbit coupling splits the originally twofold (fourfold with spin) degenerate valence band at the Γ point into two (doubly spin degenerate) bands which are separated by the spin-orbit split-off gap of $\Delta_{so} = 350$ meV. As a result the maximum of the VB moves to the BZ center and the indirect band gap reduces to 1.2 eV, in agreement with earlier calculations [25,29]. The orbital degeneracy is also removed at the K point. The energy splitting of the two highest valence bands [bands 1 and 2 in Fig. 2(a)] is 170 meV. In the conduction band, the corresponding spin-orbital gaps Δ_{so} are much smaller, 59 meV at the Γ point and 5 meV at the K point.

Away from high-symmetry points, we calculate the energy shifts $\Delta_{so}^{n,m}(\mathbf{k}) = \Delta_{rel}^{n,m}(\mathbf{k}) - \Delta_{nrel}^{n,m}(\mathbf{k})$, where $\Delta_{rel(nrel)}^{n,m}(\mathbf{k})$ is the energy difference between the bands n and m obtained from the relativistic (nonrelativistic) calculation. It provides information about the shift of the bands upon turning on SOC, with respect to their initial energy. This can be partially translated into the strength of the direct spin-orbit interaction between bands m and n , relative to the total SOC in the band m coming

TABLE I. Spin-orbital energy shifts $\Delta_{so}^{n,m}$ at high-symmetry points extracted from first-principles calculations.

k point	Γ (PBE)	K (PBE)	Γ (HSE)	K (HSE)
$\Delta_{so}^{4,5}$ [meV]	59	5	113	19
$\Delta_{so}^{1,2}$ [meV]	350	170	373	58
$\Delta_{so}^{2,3}$ [meV]	-4	-24	-9	41

from all possible couplings. Considering that SOC leads to band repulsion, positive $\Delta_{so}^{n,m}$ means that the direct spin-orbit interaction between the bands n and m is likely dominant (with respect to couplings to other bands). Analogously, if $\Delta_{so}^{n,m}$ is negative, the spin-orbit interaction between the bands n and m is weak enough to be overcome by couplings to others. Note that $\Delta_{so}^{n,m} = 0$ does not mean $\langle \psi_n | H_{so} | \psi_m \rangle = 0$. Rather, it says that the direct SOC between bands m and n is of the same order as their couplings to the other bands, and no change in energy is observed.

The results for three valence bands and two conduction bands labeled in Fig. 2(a) respectively 1, 2, 3, and 4, 5, are shown in Figs. 2(c)–2(e) and in Table 1. We have checked, by tracing the irreducible representations of the bands and applying the group theory methods, that for all $\Delta_{so}^{n,m}$ s shown in Figs. 2(c)–2(e) the direct SOC between bands n and m is allowed by the symmetry. For the valence bands 1–3, $\Delta_{so}^{n,m}(\mathbf{k})$ is strongly momentum dependent and takes significantly larger values than $\Delta_{so}^{4,5}$ in the conduction band. In the presented k -points range it varies from -180 meV for $\Delta_{so}^{2,3}(\mathbf{k})$ [Fig. 2(e)] up to 350 meV for $\Delta_{so}^{1,2}(\mathbf{k})$ [Fig. 2(d)]. In comparison, $\max(|\Delta_{so}^{4,5}|) = 59$ meV. The weaker k dependence of $\Delta_{so}^{4,5}$ results from strong isolation of the bands 4 and 5, by ~ 1.3 eV from lower and upper manifolds (not shown), effectively limiting the possible couplings mainly to those two partners.

Spin mixing. Apart from the spectroscopic features discussed above, the strength of SOC of inversion-symmetric crystals is measured by the spin mixing parameter $b_{\mathbf{k}}^2$. Because $b_{\mathbf{k}}^2$ originates from the intrinsic SOC, it constitutes a good measure of this interaction in the band structure [47]. Exceptions are spin *hot spots* formed around high-symmetry and accidental degeneracy points at which the value of $b_{\mathbf{k}}^2$ is strongly enhanced [40,47], and the mixing reaches the value of one-half (equal probability for spin up and down in a given state), irrespective of the strength of SOC.

For an arbitrary Bloch state

$$\Psi_{n,\mathbf{k}}^{\uparrow}(\mathbf{r}) = [a_{n,\mathbf{k}}(\mathbf{r})|\uparrow\rangle + b_{n,\mathbf{k}}(\mathbf{r})|\downarrow\rangle]e^{i\mathbf{k}\cdot\mathbf{r}}, \quad (4)$$

where n is the band index, $a_{n,\mathbf{k}}$ and $b_{n,\mathbf{k}}$ are lattice periodic functions, $|\sigma\rangle$, $\sigma = \{\uparrow, \downarrow\}$ is an eigenstate of spin one-half operator, and \mathbf{k} is the crystal momentum, the spin mixing parameter is defined as

$$b_{\mathbf{k}}^2 = \int |b_{n,\mathbf{k}}(\mathbf{r})|^2 d\mathbf{r}, \quad (5)$$

where the integral is taken over the entire unit cell. Here the amplitudes $a_{n,\mathbf{k}}(\mathbf{r})$ and $b_{n,\mathbf{k}}(\mathbf{r})$ are chosen in a way that $b_{n,\mathbf{k}}(\mathbf{r})$ is the amplitude of the spin component admixed by the SOC. Such a choice is possible for any spin quantization axis

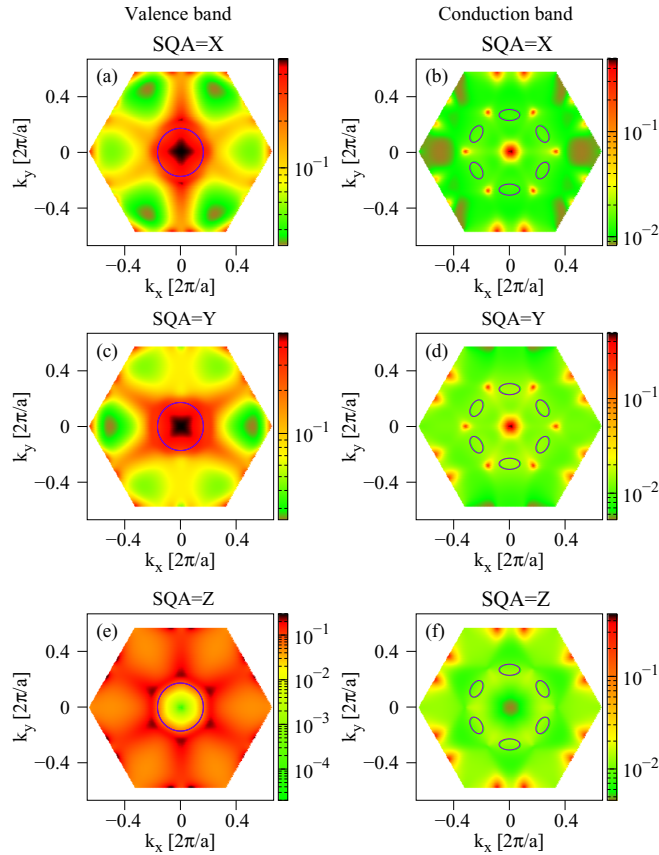


FIG. 3. Distribution of the spin mixing parameter $b_{\mathbf{k}}^2$ in the first Brillouin zone of PtSe₂ for three spin quantization axes. Left column: valence band and SQA = X (a), valence band and SQA = Y (c), valence band and SQA = Z (e). Right column: same as left but for the conduction band. Blue circles and ellipses encircle wedges of the BZ corresponding to the carried density up to $n = 12 \times 10^{13} \text{ cm}^{-2}$.

(SQA). Because usually $|b_{n,\mathbf{k}}(\mathbf{r})| \ll |a_{n,\mathbf{k}}(\mathbf{r})|$, the state (4) can still be called a *spin-up* state (although it is not an eigenstate of a Pauli matrix) [19]. For centrosymmetric systems with time-reversal symmetry, the energy degenerate *spin-down* partner of $\Psi_{n,\mathbf{k}}^{\uparrow}(\mathbf{r})$ is

$$\Psi_{n,\mathbf{k}}^{\downarrow}(\mathbf{r}) = [a_{n,-\mathbf{k}}^*(\mathbf{r})|\downarrow\rangle - b_{n,-\mathbf{k}}^*(\mathbf{r})|\uparrow\rangle]e^{i\mathbf{k}\cdot\mathbf{r}}, \quad (6)$$

and the same definition of $b_{\mathbf{k}}^2$ can be used. It is immediately seen that for normalized states $b_{\mathbf{k}}^2 \in [0, 0.5]$, where $b_{\mathbf{k}}^2 = 0$ means no spin mixing and $b_{\mathbf{k}}^2 = 0.5$ for fully spin mixed states. Alternatively, $b_{\mathbf{k}}^2$ can be defined as a deviation of the spin expectation value from one-half [48].

To quantify anisotropies in the spin relaxation and spin transport in the crystal, it is instructive to study the spin admixture parameter for different spin quantization axes, which correspond to either the direction of an applied magnetic field or to the orientation of the injected spin in a spin injection experiment. In Fig. 3 we show $b_{\mathbf{k}}^2$ calculated in the first Brillouin zone (FBZ) for the highest valence and first conduction bands, and for three different spin quantization axes SQA = {X, Y, Z} aligned with the real-space axes shown in Fig. 1. A strong anisotropy of b^2 is evident. In the valence band and for SQA = X/Y [Figs. 3(a) and 3(c)] the region

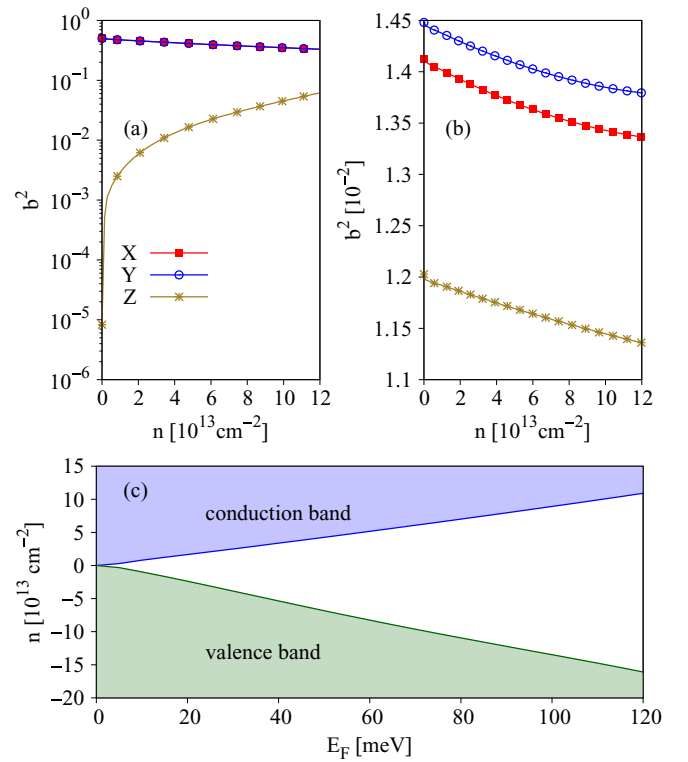


FIG. 4. Calculated Fermi-surface-averaged spin mixing parameter b^2 vs carrier density n for the valence (a) and for the conduction band (b). (c) Carrier density vs position of the Fermi level given with respect to valence-band maximum and conduction-band minimum.

around the BZ center is a spin hot region where $b_{\mathbf{k}}^2$ is close to one-half. This region is very wide and extends towards the M points, in a different way for SQA = X and SQA = Y. At the Γ point spins are fully mixed, $b_{\mathbf{k}}^2 \approx 0.5$; this is a witness to the lifting of the orbital degeneracy by SOC. For SQA = Z [Fig. 3(e)], the entire FBZ is a spin hot region with the value of $b_{\mathbf{k}}^2 \sim 10^{-2} - 10^{-1}$. An exception is a small circular wedge in the center of BZ corresponding to the vicinity of the valence-band maximum [see Fig. 2(a)]. In this wedge $b_{\mathbf{k}}^2$ varies from 10^{-5} in the center to 10^{-2} at the edge.

In the conduction band [Figs. 3(b), 3(d), and 3(f)] we observe a much smaller variation of spin mixing parameter than for the valence band. The value of $b_{\mathbf{k}}^2$ is of the order of 10^{-2} within the whole BZ, except for several spin hot spot regions localized around high symmetry and accidental degeneracy points.

According to Elliott [35], the spin mixing parameter can be translated into the spin relaxation rate, provided we know the momentum relaxation time. The latter strongly depends on temperature, concentration of defects and dopants, and for a given sample can be determined from transport experiments. Here we calculate the intrinsic, sample-independent property of PtSe₂ required to estimate spin lifetime—the Fermi-surface-averaged spin mixing parameter b^2 . It is shown in Figs. 4(a) and 4(b) as a function of carrier density n , plotted versus Fermi energy in Fig. 4(c). As can be seen, b^2 in the valence band displays a qualitatively different behavior for in-plane and out-of-plane SQA [Fig. 4(a)]. For SQA = Z it

is growing exponentially from $b^2 \approx 10^{-5}$ to $b^2 = 10^{-1}$ when the hole density is increasing. For in-plane spin polarization b^2 slowly decreases from the value of about 0.5 with increasing n but never gets below 10^{-1} . Similar doping dependence of b^2 was observed in stanene, bismuthene, and antimonene [47]. This unusually large value of b^2 is due to the very broad spin hot region close to the VB maximum. In this case the perturbative Elliott's approach to τ_s is not valid, and the spin relaxation rate is essentially the same as momentum relaxation. Therefore if the momentum relaxation anisotropy (in the plane) is not very large, one should expect a giant, doping-dependent anisotropy of the spin relaxation in PtSe₂ for holes.

In contrast, the spin relaxation anisotropy is predicted to be rather weak for conduction electrons. Indeed, as seen in Fig. 4(b), b^2 in the conduction band varies very little with n , similarly to what was observed in phosphorene, antimonene, or arsenene [47,49]. Its value is of the order of 10^{-2} , meaning that out of all momentum scattering events about 1% constitute a spin flip. Moreover, there is a very weak dependence of the spin mixing probability on SQAs. The spin relaxation rate for out-of-plane spins is expected to be somewhat slower than for in-plane spins. Also, spin lifetimes of electrons should be 1–2 orders longer than for holes, for in-plane spins.

B. Extrinsic spin-orbit coupling

In realistic situations monolayers are often encapsulated in protective layers, sit on a substrate, or are studied in a gating electric field. In any of these configurations the space inversion symmetry is broken, leading to lowering of symmetry— $D_{3d} \rightarrow C_{3v}$ in the case of monolayer PtSe₂. The spin degeneracy $\varepsilon_{\mathbf{k},\uparrow} = \varepsilon_{\mathbf{k},\downarrow}$ is lifted, except at the time-reversal points Γ and M, giving nonzero Rashba spin splitting $\Delta_{\text{so}}^R(\mathbf{k}) = \varepsilon_{\mathbf{k},\uparrow} - \varepsilon_{\mathbf{k},\downarrow}$. The emerging spin-orbit fields $\Omega_{\mathbf{k}}$ enable the D'yakonov-Perel mechanism of spin relaxation, which coexists with the Elliott-Yafet spin-flip scattering mechanism.

Encapsulating PtSe₂ by hBN is perhaps ideal to study the extrinsic effects, as the proximity-induced SOC from it is expected to be weak. A recent calculation of graphene/hBN finds the induced couplings to be on the order of $10 \mu\text{eV}$ [50], which is much below the meV scale for PtSe₂. Thus one can really explore the spin physics in hBN encapsulated PtSe₂, with top and back gates providing both doping and electric field tuning.

We model the effects of space inversion symmetry breaking by applying a uniform external electric field E in the direction perpendicular to the PtSe₂ sheet. In this approach the spin-orbit field depends on both the momentum and electric field and is related to the spin splitting as

$$H_{\text{soc}}(\mathbf{k}) = \frac{\hbar}{2} \Omega_{\mathbf{k}}(E) \cdot \boldsymbol{\sigma}, \quad (7)$$

where \hbar is the Planck constant, and $\boldsymbol{\sigma}$ is the vector of Pauli matrices.

In Figs. 5(a) and 5(b) we show $\Delta_{\text{so}}^R(\mathbf{k})$ close to the valence and conduction band edges, respectively. In the VB it displays a strong nonlinear dependence on crystal momentum. We found that close to the Γ point $\Delta_{\text{so}}^R(k) \approx 0.196 |k|^3 E \text{ meV/V nm}^{-1}$, where E is the amplitude of the

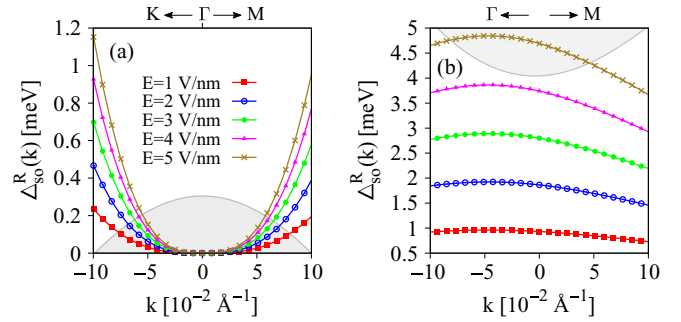


FIG. 5. Extrinsic SOC in PtSe₂: (a) spin splitting along the high-symmetry lines ($K\Gamma$ and ΓM) close to the valence-band maximum; (b) spin splitting along the ΓM line close to the conduction-band minimum. The values of k are given with respect to the VB maximum (CB minimum). The gray filled parabola sketches VB and CB close to the band gap with the band maximum/minimum centered at $k = 0$.

electric field. The spin splitting close to the CB minimum is of order of single meV and is not as much momentum dependent as in the VB. Interestingly, the maximum of $\Delta_{\text{so}}^R(\mathbf{k})$ does not coincide with the CB minimum [Fig. 5(b)]. Instead, it is shifted towards the Γ point and coincides with the position of anticrossings of bands marked 1 and 2 in Fig. 2 where the direct band gap has a global minimum (a similar shift towards the Γ point was observed for b_k^2 , not shown here). The average spin splitting in PtSe₂ is of meV range and varies between 0.1 and 50 meV, depending on E and carrier density (see Fig. 1 in [51]). Thus it is unlikely that electric field can be used to control the semiconductor-to-metal transition in PtSe₂. In fact, for $E = 6 \text{ V/nm}$ the gap decreases by only 6 meV from the initial value 1.2 eV (see Fig. 2 in the Supplemental Material [51]).

In Figs. 6(a) and 6(b) we show spin textures of the upper spin split valence band and for the lower spin split conduction band, respectively, and for the external electric field $E = 1 \text{ V/nm}$. The in-plane spin components (arrows) display a Rashba-like helical pattern, while the out-of-plane components (color) show the spin-valley locking effect [52]. Similar spin textures have been reported to exist as a result of hidden spin polarization of spin degenerate bands in PtSe₂ [31]. In contrast to layer-resolved spin textures picturing a local Rashba effect [31], Figs. 6(a) and 6(b) show a global spin texture of the entire crystal structure. The presented spin textures can be reproduced by the C_{3v} Rashba Hamiltonian containing linear and cubic terms [53], the latter being dominant. However, within the two-band model we were able to get only qualitative agreement with the DFT data. A quantitative agreement would probably require a formulation of the multiband model, taking into account all peculiarities of the band structure and the interband couplings discussed above.

To answer the question about the origin of the presented spin textures we performed calculations at an infinitesimal (numerically) electric field $E = 10^{-6} \text{ V/nm}$ in order to break space inversion symmetry but still approximately preserve the spin degeneracy. The obtained textures (Fig. 3 in the Supplemental Material [51]) resemble similar features as those shown in Figs. 6(a) and 6(b). This indicates that such a texture is intrinsic to the PtSe₂ crystalline structure and

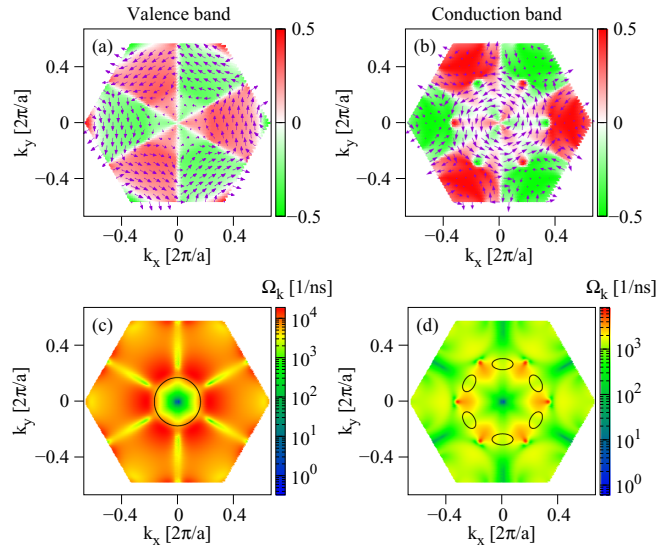


FIG. 6. Extrinsic SOC in PtSe₂. (a) In-plane spin texture (arrows) and out-of-plane spin component (color) of one spin subband of the topmost valence band plotted in the whole FBZ. (b) Same as (a) but for the bottom-most conduction band. (c) The distribution of the spin-orbit field $\Omega_{\mathbf{k}}$ in the FBZ for the valence band for the electric field $E = 1$ V/nm. (d) Same as (c) but for the conduction band. Black circle and ellipses encircle wedges of the BZ corresponding to the carried density up to $n = 12 \times 10^{13} \text{ cm}^{-2}$.

appears immediately once the space inversion symmetry is broken.

Let us now discuss the spin-orbit field $\Omega_{\mathbf{k}}$. In Figs. 6(c) and 6(d) and Fig. 7 we show the \mathbf{k} -point resolved ($\Omega_{\mathbf{k}}$) and Fermi-surface-averaged (Ω) spin-orbit fields, respectively. In the valence band the overall value of $\Omega_{\mathbf{k}}$ in the FBZ is greater than in the conduction band. This can be seen by comparing the amount of the red shaded area in Figs. 6(c) and 6(d). A very characteristic hexagonal structure is formed close to the BZ center, with corners pointing towards the M points. In this region, and also along the paths ΓM and around the K points, the spin splitting for $E = 1$ V/nm is less than 4 meV (the maximal value in the valence band and $E = 1$ V/nm is 14 meV). This gives $\Omega_{\mathbf{k}} \sim 5 \times 10^3 \text{ ns}^{-1}$, which is roughly the value of Ω for n between $8 \times 10^{13} \text{ cm}^{-2}$ and $12 \times 10^{13} \text{ cm}^{-2}$ [see the red line in Fig. 7(a)]. Within the full doping range (without the first $0.5 \times 10^{13} \text{ cm}^{-2}$), Ω in the VB varies by an order of magnitude.

In the conduction band the extrinsic SOC is weaker than in the VB, resulting in smaller values of $\Omega_{\mathbf{k}}$ [Fig. 6(d)]. For the same level of doping, e.g., $n = 10^{14} \text{ cm}^{-2}$, the ratio of Ω in the VB to Ω in the CB, $\Omega_{\text{VB}}/\Omega_{\text{CB}} \approx 3$.

Similarly to b^2 , Ω in the conduction band shows weaker doping dependence than in the VB [Fig. 7(b)]. For $E = 1$ V/nm it is of the order of 10^3 ns^{-1} and grows approximately with a step $1.5 \times 10^3 \text{ ns}^{-1}$ per 1 V/nm.

C. Spin lifetime

To estimate spin lifetimes $\tau_{s,\text{EY}}$ and $\tau_{s,\text{DP}}$ we need to know the momentum relaxation time τ_p . Taking the experimental value of the mobility for electrons $\mu = 400 \text{ cm}^2 \text{ V}^{-1} \text{ s}^{-1}$

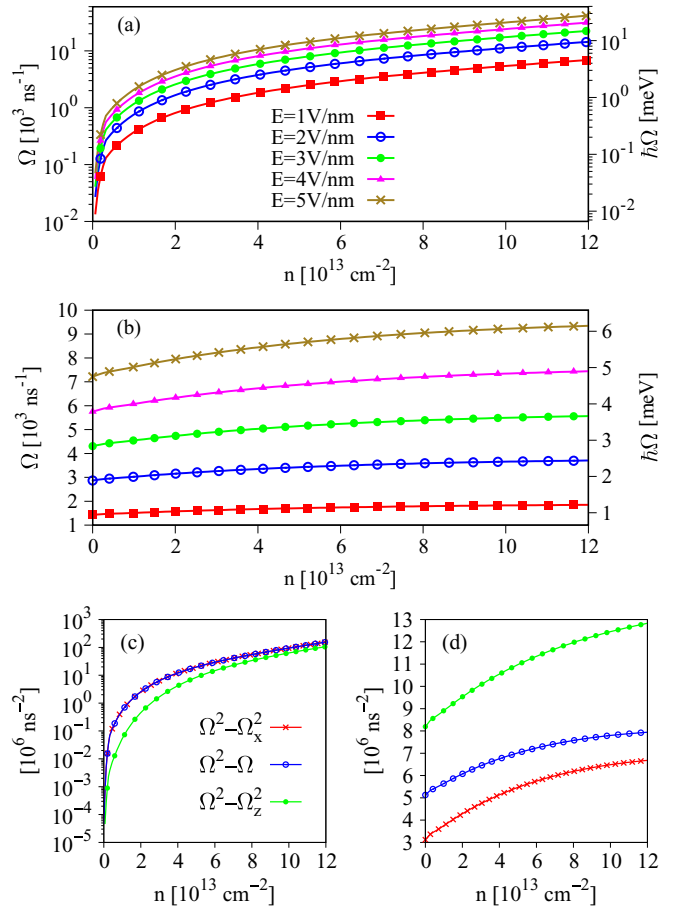


FIG. 7. Spin-orbit fields in PtSe₂. (a) Fermi-surface-averaged spin-orbit field Ω vs carrier density n and for several values of electric field for the valence band. (b) Same as (a) but for the conduction band. (c, d) Components of Ω^2 for $E = 2$ V/nm for VB and CB, respectively.

(100 K) and effective mass $m^* = 0.37m_e$ [25], we estimate, using the Drude formula $\tau_p = \mu e/m^*$, $\tau_p \approx 80$ fs, similar to other TMDs [54]. The formula (1) for the Elliott-Yafet spin relaxation rate is valid under the assumption that b^2 can be treated as a small parameter, $b^2 \ll 1$ [35]. For valence electrons being polarized in plane with the PtSe₂ sheet (SQA = X/Y), b^2 is of the order of 1 [Fig. 4], and thus Eq. (1) cannot be applied. In such a case, due to very strong spin mixing, spin lifetime should be limited by the momentum relaxation time, i.e., $\tau_{s,\text{EY}} \approx \tau_p \approx 80$ fs. For spins of valence electrons being polarized out of plane (SQA = Z) and for conduction electrons, $b^2 \approx 10^{-2}$, within the perturbative limit. The corresponding spin lifetime estimated from Eq. (1) is $\tau_{s,\text{EY}} \approx 1$ ps.

Two different regimes of spin relaxation apply also for the D'yakonov-Perel mechanism. For $E \lesssim 3$ V/nm and $n \lesssim 3 \times 10^{13} \text{ cm}^{-2}$ for the VB and for $E \lesssim 3$ V/nm for the CB we are in the motional narrowing regime, i.e., $\tau_p \Omega \ll 1$. In this case the i th component of magnetization decays proportionally to $\Omega_{\perp,i}^2 = \Omega^2 - \Omega_i^2$ [see Eq. (2)] [19]. We extract the components Ω_i , $i = x, y, z$ of the spin-orbit field according to the formula

$$\Omega_{\mathbf{k},i} = \frac{\Delta_{\text{so}}}{\hbar} \frac{s_i}{|s|}, \quad (8)$$

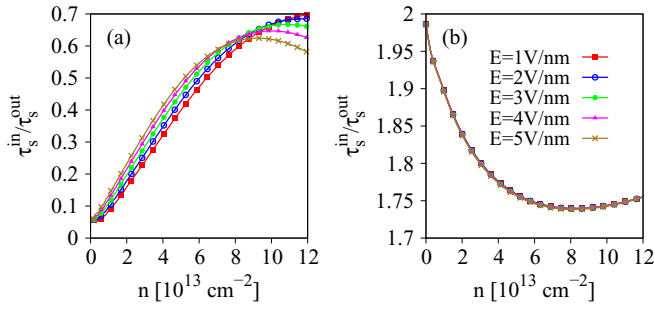


FIG. 8. D'yakonov-Perel spin lifetime anisotropy. Isotropic momentum relaxation time τ_p has been assumed.

where s_i , $i = \{x, y, z\}$ is the expectation value of spin one-half operator at a given k point. In Figs. 7(c) and 7(d) we show $\Omega_{\perp,i}^2$ for $E = 2$ V/nm for the VB and CB, respectively. A qualitative difference between the spin-orbit field in the VB and CB is evident. In the former, Ω_z has the major contribution to Ω and thus $\Omega_{\perp,z}^2$ is much smaller, even ten times, than $\Omega_{\perp,x}^2$ and $\Omega_{\perp,y}^2$ (see also Fig. 4(a) in the Supplemental Material [51]). This is consistent with the spin texture shown in Fig. 6(a): the in-plane spin components around the BZ center are very small compared to the out-of-plane ones, indicating that electron states are mainly s_z polarized. As a consequence, $\tau_{s,DP}$ is strongly anisotropic and the in-plane spins are expected to relax much faster than the out-of-plane ones [Fig. 8(a)], similar to the Elliott-Yafet mechanism. Taking $\tau_p = 80$ fs we get, for $E = 2$ V/nm and $n \approx 2 \times 10^{13} \text{ cm}^{-2}$, $\tau_{s,DP}^z \approx 40$ ps and for the in-plane spins $\tau_{s,DP}^{x/y} \approx 12$ ps.

Since $\tau_{s,EY}$ and $\tau_{s,DP}$ are anisotropic, the Elliott-Yafet and D'yakonov-Perel mechanisms can be experimentally distinguished from spin scattering by random magnetic impurities, which leads to isotropic spin relaxation [55,56]. In the CB the situation is reversed: $\Omega_{\perp,x}^2$ and $\Omega_{\perp,y}^2$ are roughly twice as big as $\Omega_{\perp,z}^2$, and so is the spin relaxation rate [see Fig. 8(b) in the main text and Fig. 4(b) in the Supplemental Material [51]]. For the same electric field and doping as for the VB, we estimate $\tau_{s,DP}^z \approx 1$ ps and $\tau_{s,DP}^{x/y} \approx 2.5$ ps. For high electric fields, when $\Omega \approx 10^4 \text{ ns}^{-1}$, the condition for motional narrowing breaks down, and the irreversible spin randomization occurs in the time scale given by the momentum relaxation, $\tau_{es,DP} \approx \tau_p \approx 80$ fs [19], irrespective of spin polarization.

Let us briefly compare PtSe₂ with other TMDs. Due to different symmetry, D_{3h} [52] instead of D_{3d} , the spin dynamics in 2H-type monolayer TMDs, such as WS₂, MoS₂, or WSe₂, is qualitatively different from than in 1T-PtSe₂. First, the in-plane mirror symmetry of the 2H crystalline structure allows only the s_z component of spin, similar to the case of flat graphene [47,57]. Second, the broken space inversion symmetry leads to the splitting of the spin states, which have opposite spin polarization at K and K' valleys due to time-reversal symmetry [52]. In effect, elastic momentum scattering-assisted spin flip is suppressed by the spin-valley coupling because the intervalley process requires a large crystal momentum variation [52,54,58–60]. The intervalley process can be accompanied by the intravalley spin scattering, in which the

electron-phonon [60] or electron-electron interactions play important roles [59,61,62]. For both types of processes, the D'yakonov-Perel mechanisms are more prominent than the Elliott-Yafet [59,61,62]. Depending on material, doping, and measurement technique, spins in monolayer 2H-TMDs can live from picoseconds up to hundreds of nanoseconds [54,58–65]. Due to the intrinsic s_z polarization of bands [58,61] the out-of-plane spin polarization relaxes significantly slower than the in-plane ones [61].

On the contrary, in monolayer PtSe₂ valleys remain spin-unpolarized and are excluded from the low-energy physics near the band gap due to the large (~ 1 eV) energy distance to the band edges. Thus the intervalley scattering is absent here, and only spin relaxation mechanisms referred to as *intravalley* in the case of 2H-TMDs are present in PtSe₂. Additionally, the spin degeneracy induces strong interband spin mixing (between the degenerate bands), which makes the Elliott-Yafet spin relaxation as important as the D'yakonov-Perel mechanism, contrary to, e.g., MoS₂ [61]. Finally, none of the spin components in PtSe₂ is protected by symmetry; out-of-plane spins are not extra protected. This explains why the predicted D'yakonov-Perel spin lifetime anisotropy in PtSe₂ shown in Fig. 8 is much smaller than in the 2H-TMDs [61].

D. Comparison of PBE and HSE exchange-correlation functionals

Since the GW [45] and experimental [10] band gaps are reported to be over 2 eV, we performed calculations using hybrid HSE [44] functional to check to what extent increasing the band gap influences the spin properties of PtSe₂. The calculated band structure and values of $\Delta_{so}^{n,m}$ are shown in Table 1 and in Fig. 5 in the Supplemental Material [51]. Although the increase of the band gap is substantial, from 1.2 eV (PBE) to 2.18 eV (HSE) there are no dramatic changes to the overall topology of the band structure and to the character and strength of SOC. The spin-orbital splittings in the valence band are slightly weaker for the HSE than for the PBE functional, while for the conduction band the situation is opposite (Figs. 1(b)–1(d) in the Supplemental Material [51]). We observed similar trends for the spin mixing parameter $b_{\mathbf{k}}^2$ (Fig. 6 in the Supplemental Material [51]). Nevertheless, the differences in b^2 are up to a factor of 2, and thus the results obtained for the HSE and PBE functionals allow the same conclusions.

IV. CONCLUSIONS

We have investigated the intrinsic and extrinsic spin-orbit couplings and their influence on the electronic properties spin relaxation in monolayer PtSe₂ using first-principles calculations. We found that the intrinsic SOC is very strong and leads to a significant mixing of the spin states. The extrinsic SOC, characterized by spin-orbit fields Ω , is also expected to be large, on the order of the intrinsic one. Their interplay is manifested in comparable contributions of the Elliott-Yafet and D'yakonov-Perel mechanisms to spin relaxation. Spin lifetime in PtSe₂ is predicted to be short, on the picosecond time scale, and to a large extent is governed by the momentum relaxation time, especially at spin hot spots where the spins are fully mixed. In this context monolayer PtSe₂ is

very different from 2H TMDs, for which much longer spin lifetimes were observed. Although pristine monolayer PtSe₂ does not seem to be the perfect candidate for application in spintronic devices requiring long spin lifetimes, line defects may considerably improve spin coherence in this material [66]. On the other hand, the strong spin-orbit coupling should be manifested prominently in spin transport and spin control phenomena.

ACKNOWLEDGMENTS

This work was supported by the National Science Centre (PL) under Contract No. DEC-2018/29/B/ST3/01892, in part by the PAAD Infrastructure cofinanced by the Operational Programme Innovative Economy, Objective 2.3, and by the Deutsche Forschungsgemeinschaft (DFG, German Research Foundation), Project ID 314695032 - SFB 1277.

-
- [1] R. F. Frindt, *J. Appl. Phys.* **37**, 1928 (1966).
- [2] J. Wilson and A. Yoffe, *Adv. Phys.* **18**, 193 (1969).
- [3] L. F. Mattheiss, *Phys. Rev. B* **8**, 3719 (1973).
- [4] K. K. Kam and B. A. Parkinson, *J. Phys. Chem.* **86**, 463 (1982).
- [5] P. Joensen, R. F. Frindt, and S. Morrison, *Mater. Res. Bull.* **21**, 457 (1986).
- [6] S. Lebègue and O. Eriksson, *Phys. Rev. B* **79**, 115409 (2009).
- [7] K. F. Mak, C. Lee, J. Hone, J. Shan, and T. F. Heinz, *Phys. Rev. Lett.* **105**, 136805 (2010).
- [8] A. Kuc, N. Zibouche, and T. Heine, *Phys. Rev. B* **83**, 245213 (2011).
- [9] A. Splendiani, L. Sun, Y. Zhang, T. Li, J. Kim, C.-Y. Chim, G. Galli, and F. Wang, *Nano Lett.* **10**, 1271 (2010).
- [10] A. Ciarrocchi, A. Avsar, D. Ovchinnikov, and A. Kis, *Nat. Commun.* **9**, 919 (2018).
- [11] A. Avsar, A. Ciarrocchi, M. Pizzochero, D. Unuchek, O. V. Yazyev, and A. Kis, *Nat. Nanotechnol.* **14**, 674 (2019).
- [12] S. Mouri, Y. Miyauchi, and K. Matsuda, *Nano Lett.* **13**, 5944 (2013).
- [13] Y. Ma, Y. Dai, M. Guo, C. Niu, Y. Zhu, and B. Huang, *ACS Nano* **6**, 1695 (2012).
- [14] K. Zollner, P. E. Faria Junior, and J. Fabian, *Phys. Rev. B* **100**, 195126 (2019).
- [15] J. S. Ross, S. Wu, H. Yu, N. J. Ghimire, A. M. Jones, G. Aivazian, J. Yan, D. G. Mandrus, D. Xiao, W. Yao, and X. Xu, *Nat. Commun.* **4**, 1474 (2013).
- [16] B. Radisavljevic, A. Radenovic, J. Brivio, V. Giacometti, and A. Kis, *Nat. Nanotechnol.* **6**, 147 (2011).
- [17] L. Britnell, R. M. Ribeiro, A. Eckmann, R. Jalil, B. D. Belle, A. Mishchenko, Y.-J. Kim, R. V. Gorbachev, T. Georgiou, S. V. Morozov *et al.*, *Science* **340**, 1311 (2013).
- [18] F. Langer, C. P. Schmid, S. Schlauderer, M. Gmitra, J. Fabian, P. Nagler, C. Schüller, T. Korn, P. G. Hawkins, Steiner *et al.*, *Nature (London)* **557**, 76 (2018).
- [19] I. Žutić, J. Fabian, and S. Das Sarma, *Rev. Mod. Phys.* **76**, 323 (2004).
- [20] J. Fabian, A. Matos-Abiague, C. Ertler, P. Stano, and I. Žutić, *Acta Phys. Slovaca* **57**, 565 (2010).
- [21] A. Avsar, J. Y. Tan, T. Taychatanapat, J. Balakrishnan, G. K. W. Koon, Y. Yeo, J. Lahiri, A. Carvalho, A. S. Rodin, O'Farrell *et al.*, *Nat. Commun.* **5**, 4875 (2014).
- [22] M. Gmitra and J. Fabian, *Phys. Rev. B* **92**, 155403 (2015).
- [23] Y. Wang, L. Li, W. Yao, S. Song, J. T. Sun, J. Pan, X. Ren, C. Li, E. Okunishi, Y.-Q. Wang *et al.*, *Nano Lett.* **15**, 4013 (2015).
- [24] X. Yu, P. Yu, D. Wu, B. Singh, Q. Zeng, H. Lin, W. Zhou, J. Lin, K. Suenaga, Z. Liu, and Q. J. Wang, *Nat. Commun.* **9**, 1545 (2018).
- [25] Y. Zhao, J. Qiao, Z. Yu, P. Yu, K. Xu, S. P. Lau, W. Zhou, Z. Liu, X. Wang, W. Ji, and Y. Chai, *Adv. Mater.* **29**, 1604230 (2017).
- [26] A. Avsar, J. Tan, M. Kurpas, M. Gmitra, K. Watanabe, T. Taniguchi, J. Fabian, and B. Özyilmaz, *Nat. Phys.* **13**, 888 (2017).
- [27] H. Huang, S. Zhou, and W. Duan, *Phys. Rev. B* **94**, 121117(R) (2016).
- [28] K. Zhang, M. Yan, H. Zhang, H. Huang, M. Arita, Z. Sun, W. Duan, Y. Wu, and S. Zhou, *Phys. Rev. B* **96**, 125102 (2017).
- [29] A. Kandemir, B. Akbali, Z. Kahraman, S. V. Badalov, M. Ozcan, F. Iyikanat, and H. Sahin, *Semicond. Sci. Technol.* **33**, 085002 (2018).
- [30] X. Zhang, Q. Liu, J. W. Luo, A. J. Freeman, and A. Zunger, *Nat. Phys.* **10**, 387 (2014).
- [31] W. Yao, E. Wang, H. Huang, K. Deng, M. Yan, K. Zhang, K. Miyamoto, T. Okuda, L. Li, Y. Wang *et al.*, *Nat. Commun.* **8**, 14216 (2017).
- [32] W. Zhang, H. T. Guo, J. Jiang, Q. C. Tao, X. J. Song, H. Li, and J. Huang, *J. Appl. Phys.* **120**, 013904 (2016).
- [33] M. Zulfiqar, Y. Zhao, G. Li, S. Nazir, and J. Ni, *J. Phys. Chem. C* **120**, 25030 (2016).
- [34] S. Datta and B. Das, *Appl. Phys. Lett.* **56**, 665 (1990).
- [35] R. J. Elliott, *Phys. Rev.* **96**, 266 (1954).
- [36] Y. Yafet, in *Solid State Physics*, edited by F. Seitz and D. Turnbull (Academic, New York, 1963), Vol. 14.
- [37] M. I. D'yakonov and V. I. Perel', *Fiz. Tverd. Tela* **13**, 3581 (1971) [*Sov. Phys. Solid State* **13**, 3023 (1972)].
- [38] M. I. Dyakonov and V. I. Perel, *Phys. Lett. A* **35**, 459 (1971).
- [39] P. Monod and F. Beuneu, *Phys. Rev. B* **19**, 911 (1979).
- [40] J. Fabian and S. Das Sarma, *Phys. Rev. Lett.* **81**, 5624 (1998).
- [41] P. Giannozzi, S. Baroni, N. Bonini, M. Calandra, R. Car, C. Cavazzoni, D. Ceresoli, G. L. Chiarotti, M. Cococcioni, I. Dabo *et al.*, *J. Phys.: Condens. Matter* **21**, 395502 (2009).
- [42] P. Giannozzi, O. Andreussi, T. Brumme, O. Bunau, M. Buongiorno Nardelli, M. Calandra, R. Car, C. Cavazzoni, D. Ceresoli, M. Cococcioni *et al.*, *J. Phys.: Condens. Matter* **29**, 465901 (2017).
- [43] J. P. Perdew, K. Burke, and M. Ernzerhof, *Phys. Rev. Lett.* **77**, 3865 (1996); **78**, 1396(E) (1997).
- [44] J. Heyd, G. E. Scuseria, and M. Ernzerhof, *J. Chem. Phys.* **118**, 8207 (2003).
- [45] H. L. Zhuang and R. G. Hennig, *J. Phys. Chem. C* **117**, 20440 (2013).
- [46] L. Bengtsson, *Phys. Rev. B* **59**, 12301 (1999).
- [47] M. Kurpas, P. E. Faria Junior, M. Gmitra, and J. Fabian, *Phys. Rev. B* **100**, 125422 (2019).
- [48] B. Zimmermann, P. Mavropoulos, S. Heers, N. H. Long, S. Blügel, and Y. Mokrousov, *Phys. Rev. Lett.* **109**, 236603 (2012).

- [49] M. Kurpas, M. Gmitra, and J. Fabian, *Phys. Rev. B* **94**, 155423 (2016).
- [50] K. Zollner, A. W. Cummings, S. Roche, and J. Fabian, *Phys. Rev. B* **103**, 075129 (2021).
- [51] See Supplemental Material at <http://link.aps.org/supplemental/10.1103/PhysRevB.103.125409> for additional plots of spin-orbit fields, spin textures, band-gap variation, and for results of calculations with hybrid exchange–correlation functional.
- [52] D. Xiao, G.-B. Liu, W. Feng, X. Xu, and W. Yao, *Phys. Rev. Lett.* **108**, 196802 (2012).
- [53] S. Vajna, E. Simon, A. Szilva, K. Palotas, B. Ujfalussy, and L. Szunyogh, *Phys. Rev. B* **85**, 075404 (2012).
- [54] Y. J. Zhang, W. Shi, J. T. Ye, R. Suzuki, and Y. Iwasa, *Phys. Rev. B* **95**, 205302 (2017).
- [55] B. Raes, J. E. Scheerder, M. V. Costache, F. Bonell, J. F. Sierra, J. Cuppens, J. Van De Vondel, and S. O. Valenzuela, *Nat. Commun.* **7**, 11444 (2016).
- [56] S. Ringer, S. Hartl, M. Rosenauer, T. Völkl, M. Kadur, F. Hopperditzel, D. Weiss, and J. Eroms, *Phys. Rev. B* **97**, 205439 (2018).
- [57] C. L. Kane and E. J. Mele, *Phys. Rev. Lett.* **95**, 226801 (2005).
- [58] H. Ochoa, F. Finocchiaro, F. Guinea, and V. I. Fal'ko, *Phys. Rev. B* **90**, 235429 (2014).
- [59] L. Yang, N. A. Sinitsyn, W. Chen, J. Yuan, J. Zhang, J. Lou, and S. A. Crooker, *Nat. Phys.* **11**, 830 (2015).
- [60] Z. Wang, A. Molina-Sánchez, P. Altmann, D. Sangalli, D. De Fazio, G. Soavi, U. Sassi, F. Bottegoni, F. Ciccacci, M. Finazzi, L. Wirtz, A. C. Ferrari, A. Marini, G. Cerullo, and S. Dal Conte, *Nano Lett.* **18**, 6882 (2018).
- [61] L. Wang and M. W. Wu, *Phys. Rev. B* **89**, 115302 (2014).
- [62] H. Schmidt, I. Yudhistira, L. Chu, A. H. Castro Neto, B. Özyilmaz, S. Adam, and G. Eda, *Phys. Rev. Lett.* **116**, 046803 (2016).
- [63] N. Papadopoulos, K. Watanabe, T. Taniguchi, H. S. J. van der Zant, and G. A. Steele, *Phys. Rev. B* **99**, 115414 (2019).
- [64] M. Ersfeld, F. Volmer, P. M. M. C. de Melo, R. de Winter, M. Heithoff, Z. Zanolli, C. Stampfer, M. J. Verstraete, and B. Beschoten, *Nano Lett.* **19**, 4083 (2019).
- [65] J. Xu, A. Habib, S. Kumar, F. Wu, R. Sundararaman, and Y. Ping, *Nat. Commun.* **11**, 2780 (2020).
- [66] M. A. U. Absor, I. Santoso, N. Yamaguchi, and F. Ishii, *Phys. Rev. B* **101**, 155410 (2020).